MATERIALS SCIENCE

Anomalous interfacial stress generation during sodium intercalation/extraction in MoS_2 thin-film anodes

Zhi Li[1]*†, Keren Jiang[1]*, Faheem Khan[1], Ankur Goswami[1], Jun Liu[1], Ali Passian[2], Thomas Thundat[1,3]†

Although the generation of mechanical stress in the anode material is suggested as a possible reason for electrode degradation and fading of storage capacity in batteries, only limited knowledge of the electrode stress and its evolution is available at present. Here, we show real-time monitoring of the interfacial stress of a few-layer MoS_2 system under the sodiation/desodiation process using microcantilever electrodes. During the first sodiation with a voltage plateau of 1.0 to 0.85 V, the MoS_2 exhibits a compressive stress (2.1 Nm^{-1}), which is substantially smaller than that measured (9.8 Nm^{-1}) during subsequent plateaus at 0.85 to 0.4 V due to the differential volume expansion of the MoS_2 film. The conversion reaction to Mo below 0.1 V generates an anomalous compressive stress of 43 Nm^{-1} with detrimental effects. These results also suggest the existence of a separate discharge stage between 0.6 and 0.1 V, where the generated stress is only approximately one-third of that observed below 0.1 V. This approach can be adapted to help resolve the localized stress in a wide range of electrode materials, to gain additional insights into mechanical effects of charge storage, and for long-lifetime battery design.

INTRODUCTION

The emergence of electrical vehicles and power-hungry handheld personal data devices has stimulated an intensive research effort in high-capacity electrode materials for Li-ion batteries (LIBs) and Na-ion batteries (SIBs). Significant total capacity improvements have been achieved by using novel anode materials, such as silicon, tin, black phosphorus, and molybdenum disulfide (MoS_2) (*1*–*3*). Among these electrode materials, MoS_2 has attracted great attention due to its well-known two-dimensional (2D) structure and a large interlayer spacing of 6.15 Å (*4*). It has been successfully adapted as anode materials to host Li, Na, and even Mg ions (*5*). Its application in SIBs is of particular interest because of its high theoretical capacity of 670 mAh g^{-1} (*6*–*8*).

A persistent challenge in high-capacity anode materials is the mechanical stress induced by ion intercalation/extraction, which causes large volume fluctuations and eventual failure of the electrode materials (*9*, *10*). To understand the real-time structural changes in the electrode (*11*–*13*), various in situ technologies have been developed (*14*–*18*). For examples, in situ transmission electron microscopy (TEM) has been used to investigate the volume expansion and pulverization of single electrode particles (*19*–*21*). Similarly, atomic force microscopy (AFM) provides additional real-time mechanical information of electrodes, such as the formation of the solid-electrolyte interface layer and Young's modulus of the electrodes (*22*, *23*). The electrode stress state and its evolution, however, remain poorly understood. Recently, pascalammetry with operando microbattery probes was used to sense the stress in solid-state batteries (*24*). Although the stress developed in bulk electrodes/cell can be measured at the macroscale using techniques such as digital image correlation technology, curvature-measurement method (*25*, *26*), and fiber optic sensors (*27*), a sensitive measurement modality to explicitly probe the stress at a nanoscale due to intercalation into a 2D material has yet to be proposed.

Microfabricated cantilever sensors are suspended beams that are extremely sensitive to surface stress (*28*). They have been successfully demonstrated as sensing elements in myriads of physical, chemical, and biological sensors that include whole-cell recognition (*29*), nucleic acid hybridization (*30*), and biomarkers and small-molecule detection (*31*). Microcantilevers are ideal sensors for liquid-based applications, particularly in the static mode, where dynamic coupling between the sensor and fluid is absent (*32*). Microcantilevers have also been used for quantitative detection of the surface stress induced by an electrochemical redox process in an electrochemistry cell (*33*). Here, we use this approach to investigate the stress induced during interaction/extraction of various Na ion species in few-layer MoS_2 under electrochemical control.

RESULTS

Multistep sodiation of MoS_2 in coin cells

We have used a traditional coin cell battery setup for investigating the electrochemical performance of the MoS_2 electrodes. We fabricated two sets of batteries using 1.7-mg ball-milled MoS_2 powder (see Materials and Methods). Discharging the first cell to 0.01 V shows three well-separated discharge plateaus during the first sodiation process, as shown in Fig. 1A. The first plateau occurring at 0.9 V corresponds to the intercalation of Na^+ to form $Na_{0.5}MoS_2$ according to

$$MoS_2 + x\,Na^+ + x\,e^- \leftrightarrow Na_xMoS_2\,(x \le 0.5) \quad (1)$$

Further intercalation of 0.5 to 1.1 mol of sodium in 1 mol of MoS_2 (*34*) following the reaction

$$Na_{0.5}MoS_2 + x\,Na^+ + x\,e^- \leftrightarrow Na_{(0.5+x)}MoS_2\,(x \le 0.6) \quad (2)$$

yields the second plateau at 0.8 V. The last plateau at 0.1 V is induced

[1]Chemical and Materials Engineering, University of Alberta, Edmonton, AB, Canada. [2]Oak Ridge National Laboratory, Oak Ridge, TN, USA. [3]Department of Chemical and Biological Engineering, University at Buffalo, The State University of New York, Buffalo, NY, USA.
*These authors contributed equally to this work.
†Corresponding author. Email: zhi.li@ualberta.ca (Z.L.); thundat@ualberta.ca (T.T.)

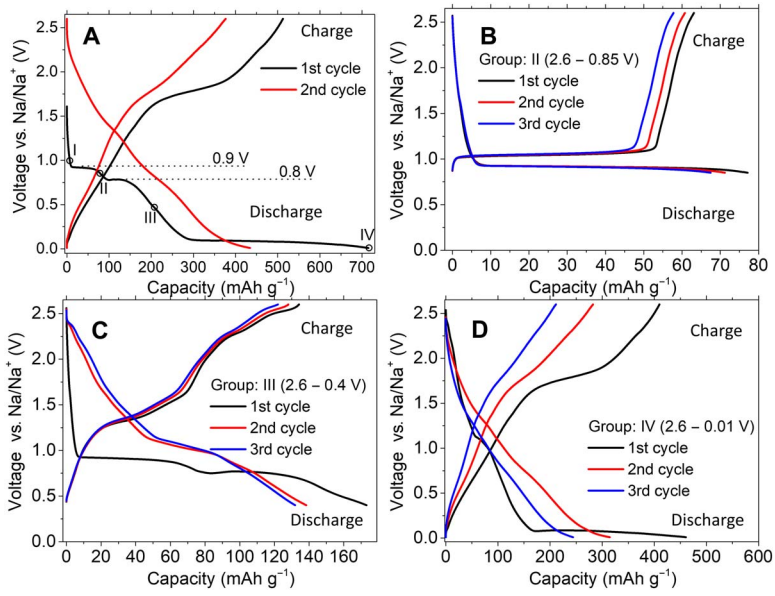

Fig. 1. Electrochemistry performance of MoS_2 evaluated in traditional coin cell battery setup. Galvanostatic charge/discharge curves of two identical MoS_2 half-cell (versus Na) coin-cell batteries at 0.05 Ag^{-1} are shown. The first battery was directly discharged to 0.01 V (**A**); the second battery was consequently discharged to 1.0 V (fig. S2), 0.85 V (**B**), 0.4 V (**C**), and 0.01 V (**D**) for three cycles each.

by the conversion reaction where MoS_2 is reduced to Mo and Na_xS according to

$$Na_{1.1}MoS_2 + 2x\,Na^+ + 2x\,e^- \leftrightarrow Mo + 2Na_{(0.55+x)}S\,(x \le 1.45) \quad (3)$$

From the second cycle onward, these plateaus blur out, and the discharge profile turns into a smooth curve. To investigate the reversibility at each stage, we subsequently cycled the second cell to four different cutoff discharge potentials (I, 1.0 V; II, 0.85 V; III, 0.4 V; and IV, 0.01 V). Above 1.0 V, the cell behaves like a highly reversible capacitor (fig. S2). The first discharge plateau at 0.9 V is reversible in all three cycles, with a corresponding charge plateau at 1.05 V (Fig. 1B). The second plateau at 0.8 V exists only in the first cycle and then turns into a smooth slope between 1.1 and 0.8 V together with the first plateau (Fig. 1C). The third discharge plateau below 0.1 V is irreversible and turns into a slope after the first cycle (Fig. 1D).

Microcantilever platform to evaluate stress evolution

The geometric features of a microcantilever make it an ideal substrate for the measurement of interfacial stress in the thin-film coating on the cantilever. By using a microcantilever with a thin layer of MoS_2 as an electrode, it is possible to quantitatively investigate the stress evolution during the sodiation/desodiation process in the MoS_2 film, as shown in Fig. 2A. To fabricate the electrode, we deposited 30 nm of silver (Ag) thin films onto both sides of the microcantilever using e-beam (electron-beam) evaporation (see Materials and Methods). As seen in the He-ion microscopy (HiM) image (Fig. 2C), a smooth silver thin film was formed on the cantilever. Later, a thin layer of MoS_2 was deposited on top of the Ag-coated microcantilevers using pulsed laser deposition (PLD), as described in Materials and Methods. As shown in Fig. 2D, the surface roughness shows a slight increase with the deposited MoS_2 film. The MoS_2 thin film was sodiated/desodiated in a custom-made electrochemical cell with a glass window that allowed continuous monitoring of the cantilever deflection (Fig. 2B). Morphological features of the surfaces were obtained by AFM topographic measurements (Fig. 2E), which revealed that the Ag films exhibit island-like characteristics composed of a distribution of nearly spherical particles with an average size of ~20 nm. Comparatively, the MoS_2 islands are significantly larger and are observed to be of quasi-hexagonal or triangular forms, which are the preferred growth structures of MoS_2 (Fig. 2F). Cross-sectional high-resolution TEM was performed to assess the layered structure of the MoS_2 thin film, as shown in Fig. 2G (described in Materials and Methods). The MoS_2 layers are parallel to the substrate. The thickness of the thin film is ~5 nm on average, or seven to eight layers. Raman spectroscopy of the MoS_2 materials, shown in Fig. 2H, demonstrates that the frequency difference between E^1_{2g} and A_{1g} peaks varies monotonously with the layer number of ultrathin MoS_2 (*35*). Compared to the peaks of bulk MoS_2 (the PLD target), the peaks of the MoS_2 thin film shifted to higher wave numbers by ~5 cm^{-1}, indicating its thickness of a few layers. Despite the marked difference in thickness, the MoS_2 target and the thin film have the same crystal structure, which was confirmed by similar x-ray diffraction (XRD) patterns acquired (Fig. 2I). In both cases, the predominant (002) peak is observed, suggesting that the basal planes of the MoS_2 are aligned in parallel with the testing surface and thus corroborating the thin-film cross-sectional TEM results.

To investigate the evolution of stress during the different stages, we cycled the cantilevers to the aforementioned four discharge cutoff potentials for three cycles each. Control experiments were also performed using an Ag-coated cantilever (defined as blank reference) under the same conditions to eliminate any possible environmental contributions to cantilever bending (e.g., ion adsorption). MoS_2 powder (~0.1 mg) was added to the base of the cantilever array as additional electrode materials in all the tests to increase the signal/noise ratio of electrochemical signals. The correlation between the voltage and the stress is evident from Fig. 3A, displaying the simultaneous acquisition of the mechanical and electric responses. The changes in

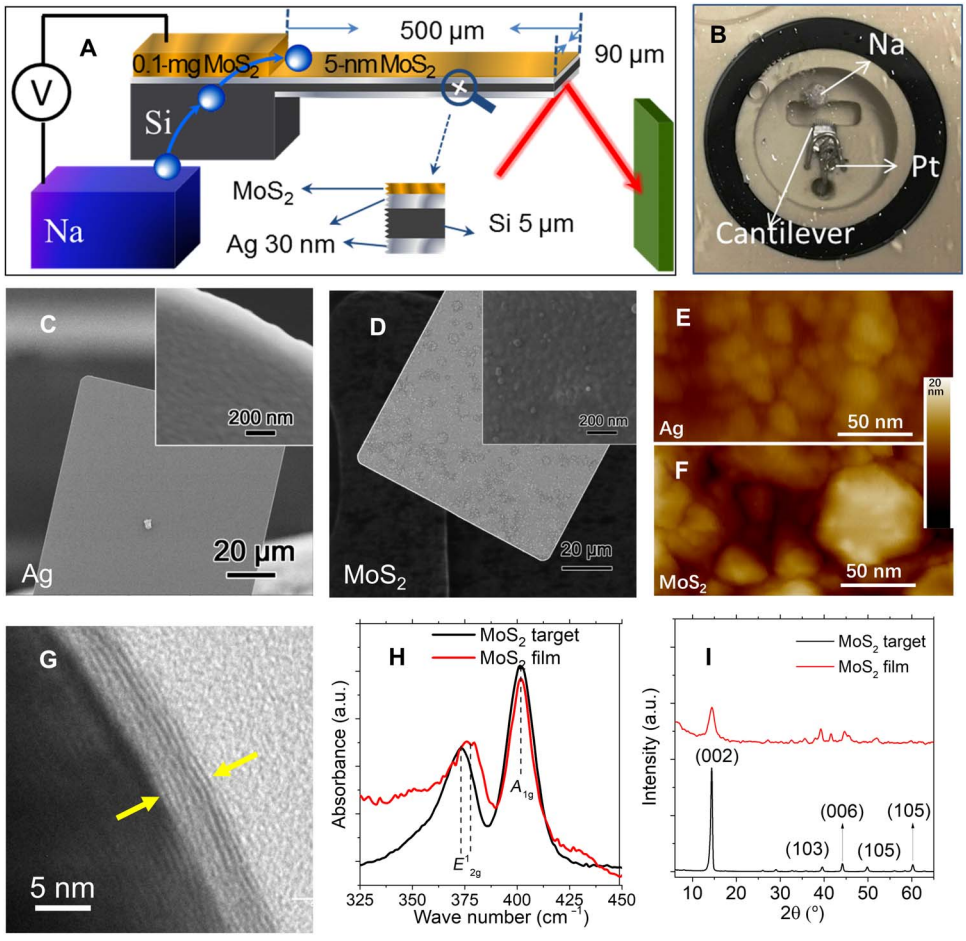

Fig. 2. Experimental setup and materials characterization. The schematic in (**A**) illustrates the microcantilever system for the detection of the sodiation/desodiation-induced stress in the few-layer MoS_2. The photograph (**B**) of the homemade electrochemistry cell shows the counter electrode made up of Na connected to a Pt wire (photo credit: Keren Jiang, University of Alberta). Morphological and chemical characterization of the electrodes was carried out by HiM (**C** and **D**), AFM (**E** and **F**), TEM (**G**), Raman spectroscopy (**H**), and XRD spectroscopy (**I**). a.u., arbitrary units.

the voltages for both cells are almost the same as they are both governed by the 0.1-mg MoS_2 on the array base, which has a mass of a few orders of magnitude higher than the MoS_2 thin film on the cantilever beam. These conditions provide nearly identical electrochemical environments, allowing a meaningful comparison of the stress developed on the cantilevers.

When immersed in the electrolyte, an electrical double layer (EDL) forms at the cantilever-electrolyte interface, leading to surface stress on the blank microcantilever. In the absence of an electrochemical redox process, this stress finds its origin in both the long-range nature of the Coulombic potential and the bulk pressure of the electrolyte (*36*). The latter can be assumed to be of the same order under both conditions of electrochemical redox on MoS_2 and without (no change in the surface area and electrolyte dielectric properties and thus the total momentum transfer to the cantilever can be assumed the same). The Coulombic contribution to the total force (or stress component) is due to the normal component of the Maxwell stress tensor in the electrostatic limit (Supplementary Materials). The EDL-induced net stress changes nearly linearly with potential (*33*, *37*), which is consistent with the measured variations in the stress of the blank cantilever with the voltage. The net stress built up on MoS_2-coated cantilever is a result of the interplay between stresses induced by EDL (voltage) and those caused by sodiation/desodiation. The latter, occurring at specific potentials, can be distinguished from the EDL contribution (varying linearly with potential) by comparing with the stress changes on the blank cantilever. The results from the differential measurements are shown in Fig. 3 (B to E), where the data have been separated into four groups of curves according to the cutoff potentials. For each group, the initial stress was shifted to zero, and the total charge/discharge time was normalized to the same scale for comparison.

Stress evolution with the cutoff potential of 1.0 V

The stress $\Delta\sigma$ on the blank cantilever, reflecting the impact of the EDL, changes with the voltage, and the observed peaks show excellent agreement, as shown in Fig. 3B. On the MoS_2-coated cantilever, $\Delta\sigma$ also follows the voltage, but with noticeable differences. First, the force direction is opposite to that of the blank cantilever. As shown in Fig. 2A, both sides of the cantilever beam are coated with silver. However, because of the deep step between the base and the cantilever, the e-beam coating process deposits significantly less silver on the side wall and possibly the hinge region, leading to a higher resistance on the bottom side of the beam. This asymmetry leads to the unbalanced EDL formation on the blank cantilever, and therefore, the overall stress changes. In contrast, the MoS_2 coating

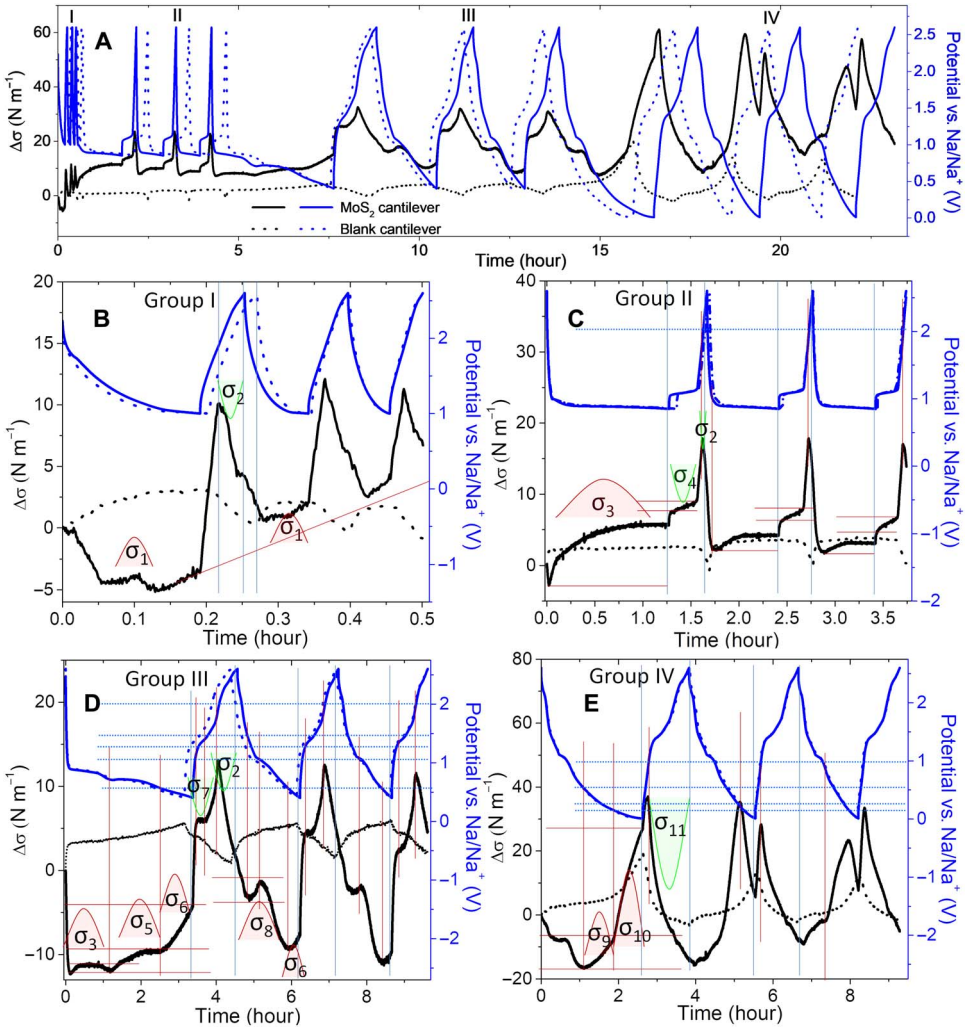

Fig. 3. Charge/discharge curves at ~0.1 Ag^{-1} (blue lines) and the synchronized stress response (black lines) of cantilever electrochemistry cells. The signals of the MoS_2-coated cantilever are shown in solid lines, and blank cantilever are shown in dotted lines. The cells are consequently discharged to 1.0 V (group I), 0.85 V (group II), 0.4 V (group III), and 0.01 V (group IV) for three cycles each. The information in whole test range is shown in (**A**), while the details in each group are shown in (**B**) to (**E**).

(semiconductor) makes the top side less conductive than the bottom side, which changes the direction of the overall effect of EDL.

Despite the opposite directions, the stress changes of both cantilevers are expected to follow the same pattern if EDL formation is the only controlling factor. However, when the cell is discharged to near 1.0 V, a small compressive stress hump (marked as σ_1, Fig. 3B) is observed, suggesting a light sodiation process, likely involving the defects in the MoS_2 thin film. This process can be confirmed by the discharging curves. When the cell voltage approaches 1.0 V, the discharge rate becomes notably slower, suggesting the existence of some noncapacitive electrochemical process. In the charging process, the cantilever develops a compressive $\Delta\sigma$ up to ~2 V, which is mainly due to the formation of EDL. The overall $\Delta\sigma$ becomes tensile afterward. This compressive/tensile transition is expected to occur at the highest voltage (2.6 V) for a pure EDL-controlled process (like the blank cantilever). Apparently, there is a tensile stress from the MoS_2 film between 2.0 and 2.6 V (marked as σ_2), which reverses the effect of EDL. This stress may be attributed to the extraction of Na from MoS_2 defect sites.

Stress evolution in the first intercalation plateau (cutoff potential of 0.85 V)

For the group II measurements (Fig. 3C), the cell was cycled between 2.6 and 0.85 V, where the intercalation of the first 0.5 mol of Na occurs (Eq. 1). In the plateau range, the cell voltage stays almost the same, and the $\Delta\sigma$ induced by EDL remains constant, just as in the case of the blank cantilever. However, for a MoS_2-coated cantilever, an increasing compressive stress (marked as σ_3) was observed in the plateau range. Since the EDL contribution does not change, the observed stress reflects the stress caused by the intercalation of Na. The measured σ_3 is ~7 Nm^{-1} in the first cycle and 2.1 and 1.5 Nm^{-1} in the following two cycles, respectively. According to the density functional theory calculation (*38*) and in situ TEM analysis (*39*), a phase transition of MoS_2 from 2H to 1T polytype also occurs in this potential range in the first cycle. The stress difference of 4.9 Nm^{-1} may reflect the phase transition–induced stress, which occurs only in the first cycle. The value of the stress in the second cycle serves as a better estimation of the true $\Delta\sigma$ caused by Na intercalation in the first plateau.

In the charging process (desodiation), the plateau range is not as flat as that observed during the discharging process. The EDL imparts a slowly increasing compressive stress on the MoS_2 cantilever (opposite to that of the blank cantilever). A tensile stress induced by Na extraction (marked as σ_4) is also expected in this range. However, this small tensile stress is buried in the compressive $\Delta\sigma$ caused by EDL. The net stress change is a small compressive stress of 1.4 Nm^{-1} in the first cycle and 1.7 and 2.2 Nm^{-1} in second and third cycles, respectively. The formation of EDL is a physical process, and its impact on stress is fairly constant in different cycles. Here, the stress trend from the blank cantilevers was used as reference to estimate the stress contribution from sodiation/desodiation process. The observed increasing net compressive stress indicates that the tensile σ_4 decreases with the cycle. A similar trend was found for σ_3.

Stress evolution in second intercalation plateau (cutoff potential of 0.4 V)

For the group III measurements, the amount of Na intercalated into MoS_2 increased to 1.1 mol. In the first discharge (Fig. 3D), two separate plateaus at 0.9 and 0.8 V were observed. As can be concluded from the behavior of the blank cantilevers, the impact of EDL on $\Delta\sigma$ causes a nearly linear and very smooth slope. The stress response of MoS_2-coated cantilever can be separated into three sections. Besides the σ_3 in the first discharging plateau (0.9 to 0.85 V), another compressive stress (marked as σ_5) was observed in the second discharging plateau (0.8 to 0.6 V). This stress of ~3.3 Nm^{-1} corresponds to the Na interaction in the second plateau. Between 0.6 and 0.4 V, a larger compressive stress of 6.5 Nm^{-1} (marked as σ_6) was observed, indicating that the last portion of Na intercalation had a higher structural impact. From an electrochemical point of view, this result is somewhat counterintuitive. Because the discharge curve is almost linear between 0.8 and 0.4 V, the value 0.4 V has been used as a common cutoff potential in all the in situ or ex situ mechanism studies (*23*, *34*, *38*, *39*). From the point of view of stress, 0.6 V is another critical point of Na intercalation.

In the charging process, the EDL initially causes a large compressive $\Delta\sigma$ with the rapid increase of the voltage. Between 1.2 and 1.5 V, $\Delta\sigma$ turns into tensile and then into compressive again. There is a tensile stress from the MoS_2 film (marked as σ_7) that counteracts the EDL contribution. From the charging curves (also see Fig. 1C), the range 1.2 to 1.5 V is where the main Na extraction occurs (slowest slope). The σ_7 can be assigned to the tensile stress of Na extraction. In the second discharge process, the two discharge plateaus at 0.8 and 0.9 V combine into a slope at ~1 V. The corresponding σ_3 and σ_5 in the first cycle combined into a compressive stress of ~3.4 Nm^{-1} (marked as σ_8).

Stress evolution in conversion reaction (cutoff potential of 0.01 V)

When the MoS_2 thin film was discharged below 0.4 V (group IV measurements), a large net compressive stress of ~43 Nm^{-1}, induced by the conversion reaction, and the EDL (tensile) effect were observed. The origin of this large stress can be explained as that from injection of up to 2.9 mol of Na into the MoS_2 film, which completely changes its structure (theoretically, it is Mo metal, rather than MoS_2). As shown in Fig. 3E, the stress change in the conversion reaction can be further separated into two sections. Before 0.1 V, the stress changes at a relatively slow rate, and the $\Delta\sigma$ is ~11 Nm^{-1} (marked as σ_9). The σ_9 is the extension of σ_6 observed in the group III test starting from 0.6 V. When the voltage reaches 0.1 V, the $\Delta\sigma$ slope becomes steeper, generating another additional 32 Nm^{-1} stress (marked as σ_{10}) before the end of the discharging process (at 0.01 V). These results suggest that the conversion reaction is composed of two separated steps with different mechanisms. A recent study based on Raman, x-ray, and TEM analyses suggests that $Na_{1.5}MoS_2$ formation (~0.1 V) is a critical point for the reversibility of the structure (*39*). Beyond that point, the MoS_2 is reduced into Mo metal. Our results explain the poor structural reversibility below 0.1 V as due to the generation of three times higher stress.

In the charging process, after a short initial period of compressive overall stress (EDL contribution), a large tensile stress (marked as σ_{11}) is developed, which dominates the overall process from 1.0 to 2.6 V. Because the first discharge to 0.01 V irreversibly changes the structure of MoS_2, the center of the sodiation-induced compressive stress shifts to a higher voltage (~0.25 V) starting from the second cycles. It also becomes smaller in the third cycle.

DISCUSSION

To recapitulate, in Fig. 4, we present a comparison of the main findings in our work with results from the in situ experimental and modeling studies of structural changes of MoS_2 reported by others. The pristine 2H-MoS_2 layer has a honeycomb structure with the single hexagonal unit cell of 6.39 Å in size and an interlayer spacing of 6.15 Å. Following the reaction given in Eq. 1, the MoS_2 accommodates ~0.5 mol of Na when sodiated to 0.85 V. A previously reported ab initio modeling study reveals that the main structural change in this process is in the axial direction, where the interlayer spacing increased to 7.42 Å, while the size of the hexagonal structure in a basal plane only changed slightly (*38*). In our investigation, the MoS_2 is grown on a silver-coated cantilever using PLD in an epitaxial manner with the basal plane parallel to the cantilever surface. The expansion in the axial direction (relative to the hexagonal structure) would not generate significant stress on the cantilever (e.g., 2.1 Nm^{-1} in the second cycle). In contrast, following Eq. 2, the intercalation of 0.5 to 1.1 mol of Na up to 0.4 V creates mainly a horizontal expansion in the basal plane for 2H-MoS_2, where the size of hexagonal structure increased to 6.58 Å, while the interlayer spacing remains almost identical (*38*). A phase transition from 2H to 1T MoS_2 is also involved in the sodiation process (*39*). Nevertheless, the expansion of 1T-MoS_2 in this potential range is also horizontal. This in-plane expansion generates a large compressive stress of 9.8 Nm^{-1} on the cantilever. According to in situ AFM studies, this stress is strong enough to distort the MoS_2 layers and induce wrinkles (*23*). In the conversion reaction range (0.4 to 0.01 V; Eq. 3), MoS_2 is converted into Mo metal particles embedded in Na_xS matrix, which has very limited reversibility. The conversion reaction generates a huge compressive stress of ~43 Nm^{-1}.

Probing the stress buildup in 2D materials is extremely important for understanding the mechanisms leading to stress and thus for optimizing the battery design. For practical applications of MoS_2, because of its limited electrical conductivity, it is often composited with some conductive substrates. The most commonly used conductive agents are various carbons. Because of the nature of the 2D materials, the basal plane of MoS_2 is often parallel to the carbon substrates. In the case of our silver-coated cantilever, it can be seen from Fig. 4 that the MoS_2 film has adapted a similar parallel configuration.

Electrochemically induced deformation of a cantilever provides fundamental insight into the stress evolution in the MoS_2 thin film during the charge and discharge stages. The obtained results suggest

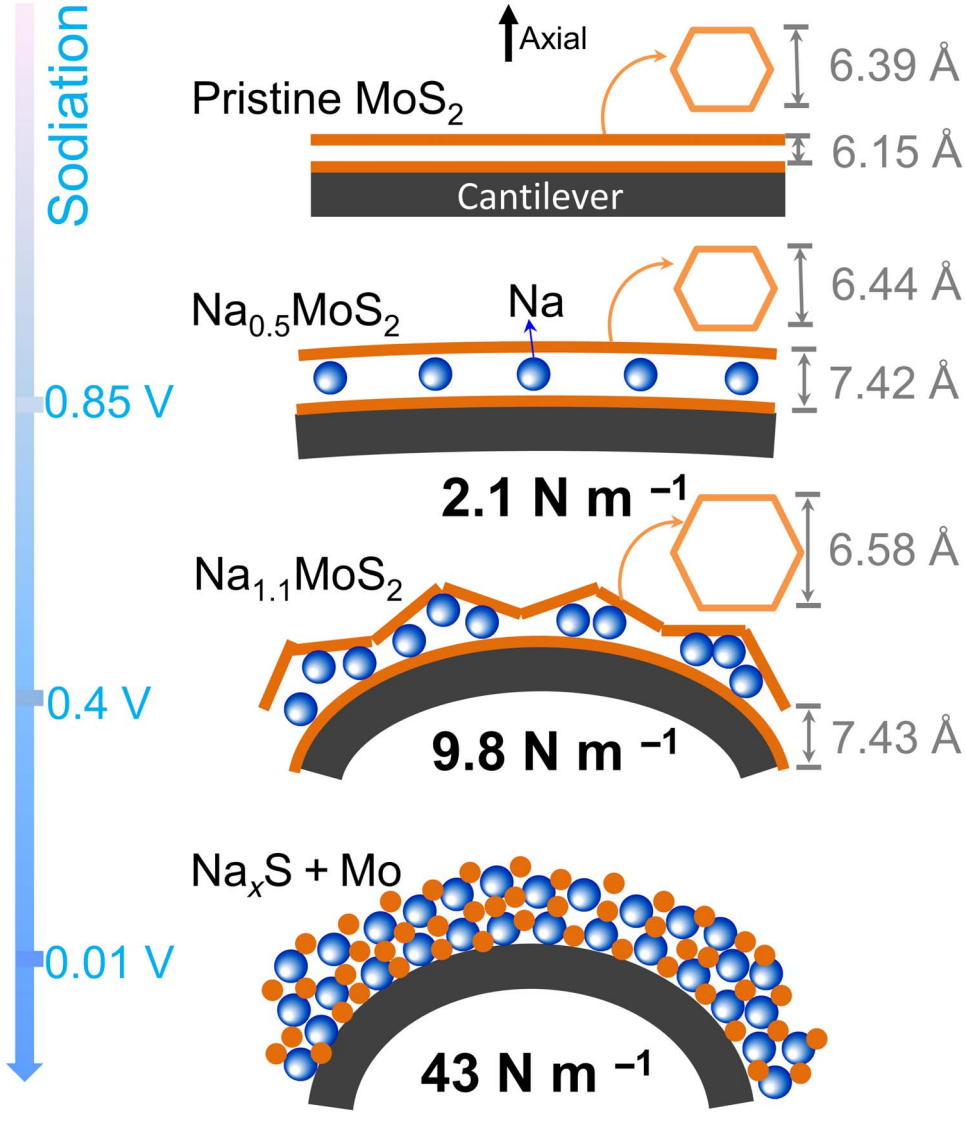

Fig. 4. A comprehensive summary of stress and structural evolution in the sodiation of few-layer MoS_2 film. The size of hexagon at upper right corner stands for the lattice size in the basal plane.

that by designing a proper electrochemical environment, the microcantilever measurement modality has the required sensitivity to distinguish the stress induced by the intercalation process from that of the EDL. From the point of view of stress, three discharge sections are suitable for Na storage, including the two discharge plateaus (0.9 and 0.8 V) and a slope range (0.6 to 0.1 V). Our results show that the discharge range below 0.1 V should be avoided since compared with the higher voltage range, it generates three times higher stress. Furthermore, we suggest using flexible conductive substrates with strong affinity to MoS_2 to accommodate the stress, especially in the basal plane.

A practical (bulk) electrode in batteries is composed of a mixture of active material, conductive agent, and binder. In the charge/discharge process, the stress builds up on each active material particle, while the binder and conductive agent partially accommodate the stress up to a certain extent. The macroscopic stress on bulk electrode/cell is the overall effect of the stress generation and adsorption in the electrode matrix, but it does not reflect the localized intrinsic stress on the active material particles. The localized stress is likely of more importance in understanding the electrode degradation because the localized degradation of the active material particles (e.g., cracking and pulverization) leads to battery failures. At bulk electrode/cell level, there may not be any noticeable difference between a functional and a failed cell. To develop a long-life electrode, it is essential to understand how the stress builds up at nano/microscale, e.g., in a nanofilm or in a single particle with different morphology, and under various charge/discharge conditions. The protocol developed in this work can be readily adapted to resolve the localized stress in a wide range of nano/microscale electrode materials and provide additional insights for electrode design and optimization.

MATERIALS AND METHODS

Coin cell battery test

MoS_2 powder (<2 μm) purchased from Sigma-Aldrich was first ball-milled with 20 weight % (wt %) carbon black and 10 wt % polyvinylidene

difluoride (binder) in *N*-methylpyrrolidone for 2 hours in a Fritsch Pulverisette 6. The well-mixed homogeneous slurry was then spread onto a copper foil using a doctor blade spreader and dried at 110°C overnight in a vacuum oven. The foil with electrode materials was then punched into circular disk electrodes about 14 mm in diameter, with ~1.7 mg of MoS_2. The active electrodes, along with a polyethene separator, the electrolytes, and Na counter electrodes, were assembled into a CR2032-type coin cell. The electrolyte is 1 M $NaClO_4$ in ethylene carbonate/diethyl carbonate (1:1). All cell assemblies were operated in an argon-filled glove box. Galvanostatic charge-discharge cycling was performed on a Solartron 1470E Multichannel Potentiostat/CellTest System.

Cantilever platform

Microcantilevers (Octosensis microcantilever arrays) were purchased from Micromotive GmbH. These arrays contain eight silicon (Si) microcantilevers on each chip (fig. S1). The beams are 500 μm in length, 90 μm in width, and 5 μm in thickness. Thirty nanometers of silver (Ag) was deposited on both sides of cantilevers with a 5-nm chromium (Cr) adhesion layer in a Kurt J. Lesker electron beam evaporator, serving as a current collector (top side) and a reflective layer (bottom side). The surface stress on the cantilever was calculated according to the Stoney equation, $\Delta Z = 3L^2(1 - \nu)\Delta\sigma/(Et^2)$, where ΔZ is the deflection, L is the length of the cantilever beam, ν is the Poisson's ratio, $\Delta\sigma$ is the surface stress, E is Young's modulus of the cantilever, and t is the thickness of the cantilever beam. The linear stress-displacement relation presented by the Stoney equation was computationally verified for our case using the full formulation of the continuum mechanics without making any approximation. For a 3D model of the cantilever with fixed-free boundary conditions, the resulting equations were solved using the finite elements method. The result is shown in fig. S4.

MoS_2 thin-film preparation

A thin layer of MoS_2 was then deposited on the top silver layer via PLD at 500°C using ultrashort (20 ns wide) pulses from an excimer laser (KrF, λ = 248 nm) with 120-mJ energy at 5-Hz repetition rate. The target used in PLD was made from the same MoS_2 powder used for the coin cell battery test. PLD is based on the photon interaction between a strong laser beam (normally in the range of millijoule) and target materials to create an ejected plume, which is collected on a substrate placed at a short distance from the target (5 cm in our experiment). Unlike thermal evaporation, e-beam evaporation, or sputtering, the laser-induced expulsion produces a plume of material with stoichiometry similar to the target. It is widely used in growing epitaxial films with stoichiometry on well-matched epitaxial substrates (*40*). It has been reported that Ag has relative matching epitaxial parameters with MoS_2 (*41*). The PLD target was made from the same MoS_2 powder used in the coin cell battery test.

Cantilever electrochemical cell

It has been well understood that LIB or SIB cells are not ideal stable systems. Because the Fermi level of Li/Na is above the lowest unoccupied molecular orbital of electrolytes, the decomposition of electrolytes cannot be fully avoided (*42*). The small amount of impurities in electrolytes also contributes some side reactions. When the mass loading of the active electrode material is high enough (1.7 mg in the coin cell), the current from side reactions can be ignored. However, the thin MoS_2 layer on one 500 μm by 90 μm cantilever is only around 1 ng; thus, its sodiation/desodiation current will be buried in the currents from side reactions. This is also a common problem for all nanobatteries used for in situ TEM and AFM studies. In this work, ~0.1 mg of additional ball-milled MoS_2 powder (the same slurry as used in coin cell test) was added to the base of the cantilever array to increase the signal/noise ratio of the electrochemical current. As shown in Fig. 2A, the MoS_2 powder on the array base and the thin film on cantilever were electrically connected. Both of them contribute current upon the intercalation/extraction of Na, but only the MoS_2 thin film on the cantilever beams leads to the bending of cantilevers. A small piece of Na metal connected to potentiostat via another platinum (Pt) wire was placed ~2 mm away from the microcantilever array and worked as the reference/counter electrode. Both electrodes were sealed in a homemade electrochemical cell (Fig. 2B) filled with electrolytes. The cell had a glass window at the top, through which a focused laser beam shone on the tip of the microcantilever, and a position-sensitive detector (PSD) was used to monitor the position shifting of the reflected laser beam. The bending of the cantilever was carefully calibrated with a laser Doppler vibrometer. In our system, 1 mV of the signal on PSD corresponds to a bending of 12.3 nm on the cantilever tip, and a surface stress difference of 73.8 mNm^{-1} according to the Stoney equation. A constant current of 10 μA was used in all the charge/discharge process, which corresponds to ~0.1 A g^{-1} according to the mass of the MoS_2.

Materials characterizations

XRD analysis of the samples was performed using a Bruker D8 Discover Diffractometer. Raman spectroscopy analysis was performed with a confocal microprobe Raman system (Thermo Nicolet Almega XR Raman microscope). Scanning HiM analysis was performed using a Zeiss Orion NanoFab equipped with Ga focused ion beam. The AFM topography was acquired using Bruker Dimension Icon system. TEM analysis was performed using a JEM-ARM200F transmission electron microscope, operating at a 200-kV accelerating voltage.

SUPPLEMENTARY MATERIALS

Supplementary material for this article is available at http://advances.sciencemag.org/cgi/content/full/5/1/eaav2820/DC1

Fig. S1. Scanning electron microscopy image of the eight-microcantilever array used in this work.

Fig. S2. Galvanostatic charge/discharge curves of MoS_2 half-cell (versus Na) batteries at 0.05 A with a cutoff discharging potential of 1.0 V.

Fig. S3. TEM cross-sectional image of continuous MoS_2 thin film in a long range.

Fig. S4. Linear displacement-stress relationship for a cantilever in response to a surface force in the direction perpendicular to the undisturbed surface.

REFERENCES AND NOTES

1. D. Kundu, E. Talaie, V. Duffort, L. F. Nazar, The emerging chemistry of sodium ion batteries for electrochemical energy storage. *Angew. Chem. Int. Ed.* **54**, 3431–3448 (2015).
2. J. Sun, H.-W. Lee, M. Pasta, H. Yuan, G. Zheng, Y. Sun, Y. Li, Y. Cui, A phosphorene–graphene hybrid material as a high-capacity anode for sodium-ion batteries. *Nat. Nanotechnol.* **10**, 980–985 (2015).
3. C. Wang, H. Wu, Z. Chen, M. T. McDowell, Y. Cui, Z. Bao, Self-healing chemistry enables the stable operation of silicon microparticle anodes for high-energy lithium-ion batteries. *Nat. Chem.* **5**, 1042–1048 (2013).
4. T. Stephenson, Z. Li, B. Olsen, D. Mitlin, Lithium ion battery applications of molybdenum disulfide (MoS2) nanocomposites. *Energy Environ. Sci.* **7**, 209–231 (2014).
5. Y. Liang, R. Feng, S. Yang, H. Ma, J. Liang, J. Chen, Rechargeable Mg batteries with graphene-like MoS_2 cathode and ultrasmall Mg nanoparticle anode. *Adv. Mater.* **23**, 640–643 (2011).
6. L. David, R. Bhandavat, G. Singh, MoS2/graphene composite paper for sodium-ion battery electrodes. *ACS Nano* **8**, 1759–1770 (2014).

7. Y. Liu, X. He, D. Hanlon, A. Harvey, J. N. Coleman, Y. Li, Liquid phase exfoliated MoS2 nanosheets percolated with carbon nanotubes for high volumetric/areal capacity sodium-ion batteries. *ACS Nano* **10**, 8821–8828 (2016).
8. W. Ren, W. Zhou, H. Zhang, C. Cheng, ALD TiO_2-coated flower-like MoS_2 nanosheets on carbon cloth as sodium ion battery anode with enhanced cycling stability and rate capability. *ACS Appl. Mater. Interfaces* **9**, 487–495 (2017).
9. X. Wang, W. Zeng, L. Hong, W. Xu, H. Yang, F. Wang, H. Duan, M. Tang, H. Jiang, Stress-driven lithium dendrite growth mechanism and dendrite mitigation by electroplating on soft substrates. *Nat. Energy* **3**, 227–235 (2018).
10. M. Wang, C. Jiang, S. Zhang, X. Song, Y. Tang, H.-M. Cheng, Reversible calcium alloying enables a practical room-temperature rechargeable calcium-ion battery with a high discharge voltage. *Nat. Chem.* **10**, 667–672 (2018).
11. Y. Gogotsi, What nano can do for energy storage. *ACS Nano* **8**, 5369–5371 (2014).
12. C. P. Grey, J. M. Tarascon, Sustainability and in situ monitoring in battery development. *Nat. Mater.* **16**, 45–56 (2017).
13. C. Prehal, C. Koczwara, N. Jackel, A. Schreiber, M. Burian, H. Amenitsch, M. A. Hartmann, V. Presser, O. Paris, Quantification of ion confinement and desolvation in nanoporous carbon supercapacitors with modelling and in situ X-ray scattering. *Nat. Energy* **2**, 16215 (2017).
14. P. P. R. M. L. Harks, F. M. Mulder, P. H. L. Notten, In situ methods for Li-ion battery research: A review of recent developments. *J. Power Sources* **288**, 92–105 (2015).
15. Q. Gu, J. A. Kimpton, H. E. A. Brand, Z. Wang, S. Chou, Solving key challenges in battery research using in situ synchrotron and neutron techniques. *Adv. Energy Mater.* **7**, 1602831 (2017).
16. J. M. Griffin, A. C. Forse, W.-Y. Tsai, P.-L. Taberna, P. Simon, C. P. Grey, In situ NMR and electrochemical quartz crystal microbalance techniques reveal the structure of the electrical double layer in supercapacitors. *Nat. Mater.* **14**, 812–819 (2015).
17. A. C. Forse, J. M. Griffin, C. Merlet, J. Carretero-Gonzalez, A.-R. O. Raji, N. M. Trease, C. P. Grey, Direct observation of ion dynamics in supercapacitor electrodes using in situ diffusion NMR spectroscopy. *Nat. Energy* **2**, 16216 (2017).
18. P. Pietsch, D. Westhoff, J. Feinauer, J. Eller, F. Marone, M. Stampanoni, V. Schmidt, V. Wood, Quantifying microstructural dynamics and electrochemical activity of graphite and silicon-graphite lithium ion battery anodes. *Nat. Commun.* **7**, 12909 (2016).
19. L. Wang, D. Liu, S. Yang, X. Tian, G. Zhang, W. Wang, E. Wang, Z. Xu, X. Bai, Exotic reaction front migration and stage structure in lithiated silicon nanowires. *ACS Nano* **8**, 8249–8254 (2014).
20. J. Y. Huang, L. Zhong, C. M. Wang, J. P. Sullivan, W. Xu, L. Q. Zhang, S. X. Mao, N. S. Hudak, X. H. Liu, A. Subramanian, H. Fan, L. Qi, A. Kushima, J. Li, In Situ observation of the electrochemical lithiation of a single SnO2 nanowire electrode. *Science* **330**, 1515–1520 (2010).
21. Z. Li, X. Tan, P. Li, P. Kalisvaart, M. T. Janish, W. M. Mook, E. J. Luber, K. L. Jungjohann, C. B. Carter, D. Mitlin, Coupling in situ TEM and Ex situ analysis to understand heterogeneous sodiation of antimony. *Nano Lett.* **15**, 6339–6348 (2015).
22. N. Balke, S. Jesse, A. N. Morozovska, E. Eliseev, D. W. Chung, Y. Kim, L. Adamczyk, R. E. García, N. Dudney, S. V. Kalinin, Nanoscale mapping of ion diffusion in a lithium-ion battery cathode. *Nat. Nanotechnol.* **5**, 749–754 (2010).
23. S. D. Lacey, J. Wan, A. von Wald Cresce, S. M. Russell, J. Dai, W. Bao, K. Xu, L. Hu, Atomic force microscopy studies on molybdenum disulfide flakes as sodium-ion anodes. *Nano Lett.* **15**, 1018–1024 (2015).
24. J. M. Larson, E. Gillette, K. Burson, Y. Wang, S. B. Lee, J. E. Reutt-Robey, Pascalammetry with operando microbattery probes: Sensing high stress in solid-state batteries. *Sci. Adv.* **4**, eaas8927 (2018).
25. V. A. Sethuraman, V. Srinivasan, A. F. Bower, P. R. Guduru, In situ measurements of stress-potential coupling in lithiated silicon. *J. Electrochem. Soc.* **157**, A1253–A1261 (2010).
26. V. A. Sethuraman, M. J. Chon, M. Shimshak, V. Srinivasan, P. R. Guduru, In situ measurements of stress evolution in silicon thin films during electrochemical lithiation and delithiation. *J. Power Sources* **195**, 5062–5066 (2010).
27. X. Cheng, M. Pecht, In situ stress measurement techniques on li-ion battery electrodes: A review. *Energies* **10**, 591 (2017).
28. R. Datar, S. Kim, S. Jeon, P. Hesketh, S. Manalis, A. Boisen, T. Thundat, Cantilever sensors: Nanomechanical tools for diagnostics. *MRS Bull.* **34**, 449–454 (2011).
29. K. Y. Gfeller, N. Nugaeva, M. Hegner, Micromechanical oscillators as rapid biosensor for the detection of active growth of Escherichia coli. *Biosens. Bioelectron.* **21**, 528–533 (2005).
30. F. Huber, H. P. Lang, N. Backmann, D. Rimoldi, C. Gerber, Direct detection of a BRAF mutation in total RNA from melanoma cells using cantilever arrays. *Nat. Nanotechnol.* **8**, 125–129 (2013).
31. J. W. Ndieyira, N. Kappeler, S. Logan, M. A. Cooper, C. Abell, R. A. McKendry, G. Aeppli, Surface-stress sensors for rapid and ultrasensitive detection of active free drugs in human serum. *Nat. Nanotechnol.* **9**, 225–232 (2014).
32. J. Fritz, Cantilever biosensors. *Analyst* **133**, 855–863 (2008).
33. F. Tian, J. H. Pei, D. L. Hedden, G. M. Brown, T. Thundat, Observation of the surface stress induced in microcantilevers by electrochemical redox processes. *Ultramicroscopy* **100**, 217–223 (2004).
34. J. Park, J.-S. Kim, J.-W. Park, T.-H. Nam, K.-W. Kim, J.-H. Ahn, G. Wang, H.-J. Ahn, Discharge mechanism of MoS_2 for sodium ion battery: Electrochemical measurements and characterization. *Electrochim. Acta* **92**, 427–432 (2013).
35. H. Li, Q. Zhang, C. C. R. Yap, B. K. Tay, T. H. T. Edwin, A. Olivier, D. Baillargeat, From bulk to monolayer MoS2: Evolution of raman scattering. *Adv. Funct. Mater.* **22**, 1385–1390 (2012).
36. S. L. Carnie, D. Y. C. Chan, The statistical mechanics of the electrical double layer: Stress tensor and contact conditions. *J. Chem. Phys.* **74**, 1293–1297 (1981).
37. D. Kramer, R. N. Viswanath, J. Weissmüller, Surface-stress induced macroscopic bending of nanoporous gold cantilevers. *Nano Lett.* **4**, 793–796 (2004).
38. M. Mortazavi, C. Wang, J. Deng, V. B. Shenoy, N. V. Medhekar, Ab initio characterization of layered MoS_2 as anode for sodium-ion batteries. *J. Power Sources* **268**, 279–286 (2014).
39. X. Wang, X. Shen, Z. Wang, R. Yu, L. Chen, Atomic-scale clarification of structural transition of MoS_2 upon sodium intercalation. *ACS Nano* **8**, 11394–11400 (2014).
40. M. I. Serna, S. H. Yoo, S. Moreno, Y. Xi, J. P. Oviedo, H. Choi, H. N. Alshareef, M. J. Kim, M. Minary-Jolandan, M. A. Quevedo-Lopez, Large-area deposition of MoS_2 by pulsed laser deposition with in situ thickness control. *ACS Nano* **10**, 6054–6061 (2016).
41. T. A. J. Loh, D. H. C. Chua, Growth mechanism of pulsed laser fabricated few-layer MoS_2 on metal substrates. *ACS Appl. Mater. Interfaces* **6**, 15966–15971 (2014).
42. J. B. Goodenough, Evolution of strategies for modern rechargeable batteries. *Acc. Chem. Res.* **46**, 1053–1061 (2013).

Acknowledgments: We acknowledge the nanoFAB facility at the University of Alberta for its materials characterization support. **Funding:** This work was supported by the Canada Excellence Research Chairs (CERC) Program. **Author contributions:** Z.L., K.J., and T.T. conceived the project. Z.L., K.J., and F.K. designed the experimental setup. Z.L. and K.J. performed the experiments, characterized the materials, and analyzed the data. A.G. performed the XRD and helped with the PLD. A.P. provided theoretical support for stress analysis. J.L. assisted with AFM characterization. Z.L. wrote the manuscript with contributions from K.J. **Competing interests:** The authors declare that they have no competing interests. **Data and materials availability:** All data needed to evaluate the conclusions in the paper are present in the paper and/or the Supplementary Materials. Additional data related to this paper may be requested from the authors.

Submitted 31 August 2018
Accepted 28 November 2018
Published 2 January 2019
10.1126/sciadv.aav2820

Citation: Z. Li, K. Jiang, F. Khan, A. Goswami, J. Liu, A. Passian, T. Thundat, Anomalous interfacial stress generation during sodium intercalation/extraction in MoS_2 thin-film anodes. *Sci. Adv.* **5**, eaav2820 (2019).

Science Advances

Anomalous interfacial stress generation during sodium intercalation/extraction in MoS_2 thin-film anodes

Zhi Li, Keren Jiang, Faheem Khan, Ankur Goswami, Jun Liu, Ali Passian and Thomas Thundat

Sci Adv **5** (1), eaav2820.
DOI: 10.1126/sciadv.aav2820